

pubs.acs.org/JPCL Letter

Effects of Surface Defects on Performance and Dynamics of CsPbl₂Br Perovskite: First-Principles Nonadiabatic Molecular Dynamics Simulations

Bao Liu, Zhaoxin Wang, Shuping Huang,* Yulun Han,* and Dmitri S. Kilin*



Cite This: J. Phys. Chem. Lett. 2024, 15, 4782–4791



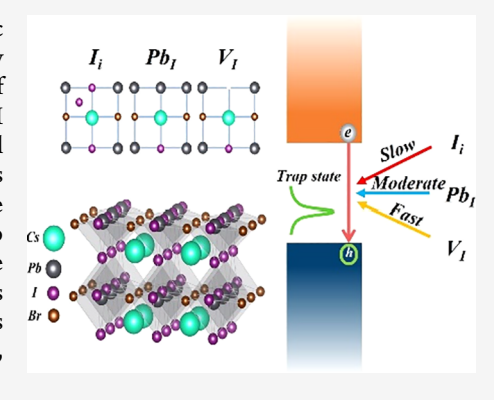
ACCESS I

Metrics & More

Article Recommendations

s Supporting Information

ABSTRACT: Inorganic mixed-halogen perovskites exhibit excellent photovoltaic properties and stability; yet, their photoelectric conversion efficiency is limited by inherent surface defects. In this work, we study the impact of defects on properties of $CsPbI_2Br$ slabs using first-principles calculations, focusing on specific defects such as I vacancy (V_I) , I interposition (I_i) , and I substitution by Pb (Pb_I) . Our findings reveal that these defects affect the geometric and optoelectronic properties as well as dynamics of charge carriers of slabs. We employ two theoretical frameworks (surface hopping and Redfield theory) of nonadiabatic molecular dynamics simulations to comprehensively study relaxation processes and obtain consistent results. The presence of V_I reduces carrier lifetimes, while the influence of Pb_I on carrier lifetimes is negligible. In contrast, I_i defects lead to prolonged carrier lifetimes. These insights provide valuable guidance for the rational design of perovskite photovoltaic devices, aiming to enhance their efficiency and stability.



ue to its ideal direct band gap, high optical absorption coefficient, significant carrier mobility, and good defect tolerance, the all-inorganic halide perovskite has received a lot of interest.¹⁻⁴ Perovskite solar cells (PSCs) now have a power conversion efficiency (PCE) of 26%,⁵ indicating its enormous promise as the next generation of low-cost solar technology. However, the two inorganic perovskites CsPbI₃ and CsPbBr₃ studied so far exhibit inherent drawbacks. Specifically, the forbidden bandwidth of CsPbI3 is 1.7 eV. The solar cell with CsPbI₃ as the photoactive layer shows the best PCE, but the crystalline structure of CsPbI3 is prone to alteration under room temperature, which affects the stability of the cell.⁶⁻⁸ CsPbBr₃ exhibits enhanced crystal structure stability; however, its wide bandgap of 2.3 eV adversely affects the generation of photogenerated carriers, leading to a low current density of the device. 9-12 On the other hand, the mixed-halide CsPbI₂Br with a bandgap value of 1.9 eV shows higher visible light absorption than CsPbBr₃ and better stability than CsPbI₃. 13-15 Due to its low exciton binding energy, electron-hole pairs can readily separate into free carriers, thus improving charge carrier generation efficiency, and recombination losses are reduced, enabling more efficient collection of generated charges at the electrodes. 16-18 Therefore, CsPbI2Br has excellent potential for application in the field of photovoltaic devices.

The currently known best PCE for CsPbI₂Br PSCs was 17.8%, ¹⁹ far from the Shockley-Quisser (S-Q) limit. ²⁰ The primary cause is the presence of defects at interiors, grain boundaries, and interfaces that create carrier recombination centers, carrier complexes, and charge accumulation. ^{21–24}

During the preparation of CsPbI₂Br thin films, it is inevitable that surface defects are formed.^{25,26} The defect density on the surface is higher by several orders of magnitude than the interior.²⁷ In typical PSCs, defects are localized at the interfaces between the active layers and the charge transport layers. 28-31 These interfacial defects introduce trap states within the bandgap, which capture charge carriers, facilitate their recombination, and reduce the amount of charge carriers reaching the electrodes, thereby reducing the photocurrent and, consequently, the efficiency of PSCs. 32,33 In addition. these defects provide ion migration channels under elevated temperatures and optical conditions, which can act as stochastic dopants, altering the bandgap width and affecting the performance of PSCs. 34-38 Charge typically builds up at defects, impeding the dispersion of the electric field within devices, which may result in an intrinsic performance loss and contribute to hysteresis in the current-voltage characteristics of PSCs. 39-42 The issues from interfacial defects will be exacerbated during scale-up for practical applications, constraining the commercialization of PSCs. 43 Understanding the impact of defects on the electronic properties and dynamics of

Received: March 3, 2024
Revised: April 13, 2024
Accepted: April 17, 2024
Published: April 25, 2024





charge carriers is important for enhancing the stability and PCE of PSCs.

In this work, we carry out first-principles calculations to systematically investigate the geometric and optoelectronic properties of $CsPbI_2Br$ surfaces with intrinsic defects. Nonadiabatic molecular dynamics (NAMD) simulations are performed to comprehensively study relaxation processes. We focus on defects with low formation energies, which are expected to be abundant during synthesis, such as I vacancy (V_I) , I interposition (I_i) , and Pb substitution for I (Pb_I) . The perovskite slabs with such defects show distinct electronic structures and electron–phonon (e-p) coupling. Additionally, a comparison is made between the Hefei-NAMD method employing surface hopping theory $^{44-46}$ and the reduced density matrix (RDM) formalism within the Redfield theory $^{47-51}$ in studying relaxation processes of charge carriers.

The cubic phase (α -phase) CsPbI₂Br is considered, which has better performance stability than the tetragonal phase (β -phase) CsPbI₂Br. The calculated lattice parameters of the α -phase CsPbI₂Br are a = c = 6.13 Å and b = 5.98 Å, consistent with the earlier findings. ^{52–54} The α -phase surface defects are constructed based on the (100) surface, which is dominant in the experimental X-ray diffraction pattern. ⁵⁵ Beyond three atomic layers, any excess layers are expected to have minimal influence on the surface. ⁵⁶ Therefore, we construct only four atomic layers and add a vacuum layer of 20 Å in the z-direction to eliminate the interaction between the periodic images.

Density functional theory (DFT) simulations are performed using the Vienna Ab initio Simulation Package (VASP)^{57,58} to optimize the geometry and investigate the surface defect characteristics. We employ an exchange-correlation functional of Perdew-Burke-Ernzerhof (PBE) generalized gradient approximation (GGA)⁵⁹ and use projected augmented wave (PAW)⁶⁰ potentials. The valence electron constituents are 5s² $5p^{6}$ 6s¹ for Cs, $5d^{10}$ 6s² 6p² for Pb, $5s^{2}$ 5p⁵ for I, and $4s^{2}$ 4p⁵ for Br. The plane wave basis set uses a kinetic energy cutoff of 450 eV, and the geometry is relaxed until the residual force per atom is less than 0.015 eV/Å⁻¹. The supercell, containing $2 \times$ 2 unit cells, provides sufficient distances to prevent interactions between defects. The molecular formula of the original supercell is Cs₈Pb₈I₁₆Br₈. For the three main studied defects, the molecular formulas are as follows: V_I (Cs₈Pb₈I₁₅Br₈), I_i (Cs₈Pb₈I₁₇Br₈), and Pb_I (Cs₈Pb₉I₁₅Br₈), see Table S1. Due to the electrostatic attraction between slabs, charged systems are not considered. 61 The Brillouin zone is sampled using a 3 \times 3 × 1 Monkhorst-Pack-point grid.

Following geometric optimization, we employ velocity tuning to raise the system temperature to 300 K. Then, using a 1 fs time step, 6 ps microcanonical ab initio molecular dynamics (AIMD) trajectories are constructed. NAMD results are obtained by averaging over 100 different initial configurations from the last 3 ps of the AIMD trajectories.

The nuclear trajectories and the Kohn–Sham (KS) orbitals obtained by VASP are used to calculate the nonadiabatic couplings (NACs). The NAC determines the probability of transitions for electrons and holes in excited states between various energy levels during the NAMD process. The time-dependent KS equations are solved in the scheme of the surface hopping method and the classical path approximation (CPA). The conduction band (CB) and valence band (VB) edges of CsPbI₂Br are located at the Γ-point, making it a direct band gap semiconductor. To save computational resources, the NAC and NAMD calculations are performed only at the Γ -

point. The obtained results from the Hefei-NAMD method are also compared with those obtained from the RDM method within the Redfield theory. The calculated results from the latter are based on NACs obtained from the former. The details of these two methods can be found in the Supporting Information.

The optimized structures and surface formation energies of CsPbI₂Br (100) with four different terminations (CsI₂, CsBr₂, PbI₂, and PbIBr) are shown in Figure S1. The PbIBr termination, which is characterized with a small surface formation energy, 72-74 is used to study the effect of defects. We calculate the defect formation energy (DFE) of the uppermost layer of the perovskite surface in the presence of point defects, including vacancies (V_{Pb}, V_L, and V_{Br}), interstitials (Pb_i, I_i, and Br_i), and antisubstitutions (Pb_{Br}, Pb_I, I_{ph}, and Br_{ph}, where A_B indicates that B is substituted by A) as shown in Figure S2. The DFE reflects the ease of defect formation with a smaller value indicating a higher likelihood for the defect to form. Among these 10 defects, we focus on the representative defects with small DFE, which are also commonly abundant in the synthesis process, namely, I vacancy (V_I), I interposition (I_i), and I substituted by Pb (Pb_1) .

We fix the lattice parameters of the original cell to optimize these point-defect structures on the CsPbI₂Br (100) surface. The optimized geometries and structural parameters are listed in Figure 1a and Table 1. The slab with the V_I defect has a

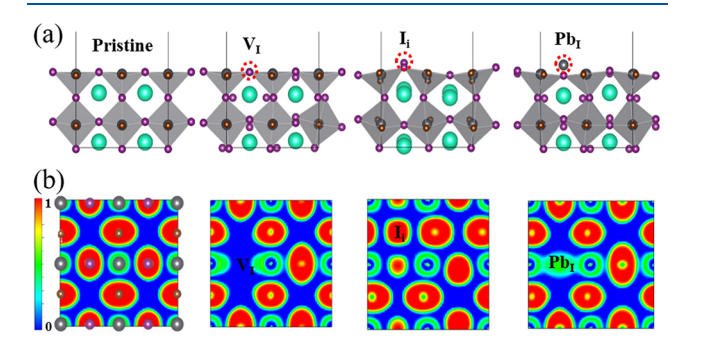


Figure 1. (a) Optimized structures and (b) surface electron densities of $CsPbI_2Br$ (100) pristine and different defective surfaces. The red circle in (a) indicates the position of the defect. The letters in (b) represent the defective atoms and their locations. The green, gray, brown, and purple spheres represent Cs, Pb, Br, and I atoms, respectively.

relatively large DFE compared to the other defects. There are minor changes observed in the average Pb–I and Pb–Br bond lengths and \angle M–X–M (M = Pb, X = I, Br) angle relative to the pristine surface. The slab with the I_i defect has a low DFE and larger surface $[PbI_3Br_2]^{3-}$ structure deformation. The

Table 1. Main Geometrical Parameters and Defect Formation Energies of CsPbI₂Br Slabs with and without Defects

	Pristine	V_{I}	\mathbf{I}_{i}	Pb_{I}
$d_{\mathrm{Pb-I}}$ (Å)	3.216	3.205	3.286	3.223
$d_{\mathrm{Pb-Br}}$ (Å)	2.996	2.995	3.053	3.008
∠Pb−I−Pb (deg)	170.9	170.3	145.0	173.6
∠Pb−Br−Pb (deg)	173.7	172.6	148.8	166.5
DFE (eV)	/	2.01	0.72	3.25

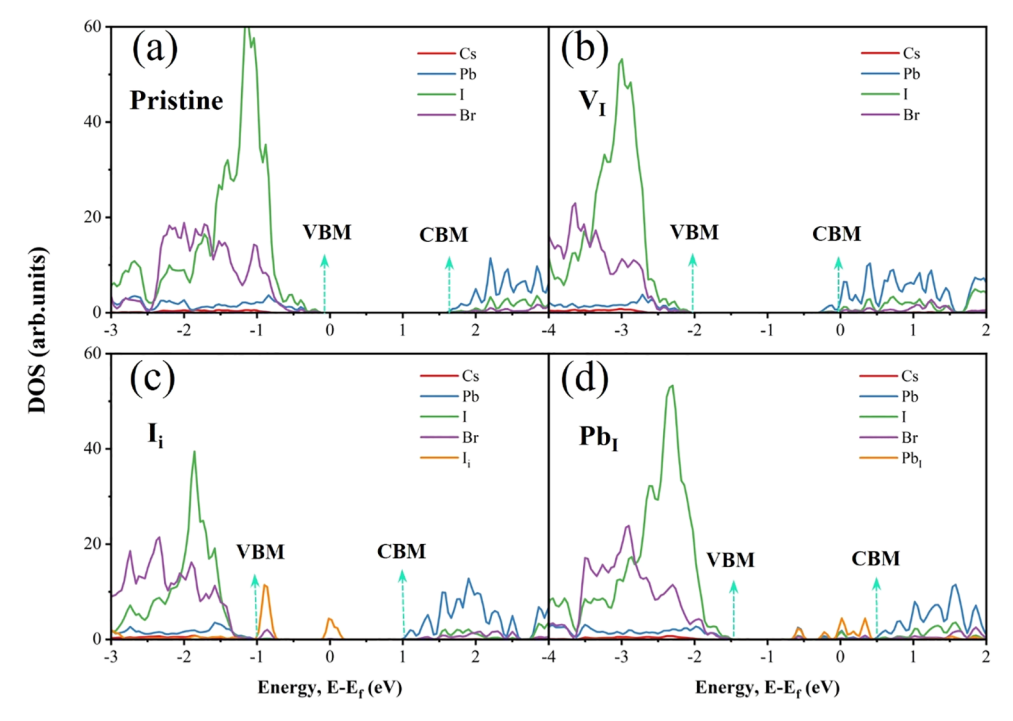


Figure 2. Elemental projected density of states for (a) pristine and (b-d) defective $CsPbI_2Br$ (100) surfaces. The energy reference is put at the Fermi energy level.

atoms around the interstitial defect move away, making the metal-halide framework more curved, as shown by the increase in the average Pb-I and Pb-Br bond lengths and the decrease in the average angle. The average distance between the defective I atom on the surface and the surrounding I atoms is 3.44 Å. For the slab with the Pb_I defect, which has a large DFE, the Pb atoms are more inclined to be located above the surface, indicating that the defect is more difficult to form. The halogen atoms around the defect are closer to the defective Pb atom as shown by the longer bond lengths and smaller bond angles. The average distance between the defective Pb atom on the surface and the surrounding Pb atoms is 3.28 Å. The distribution of electron density reflects the degree of interatomic interactions. As shown in Figure 1b, slabs with V_I and Pb_I defects, characterized by minor structural deformation, exhibit low electron densities around the defective sites and minimal changes in electron densities outside of these sites. The slab with the I_i defect, characterized by large structure deformation, exhibits enhanced interactions between the defect and surrounding atoms, thus reducing the formation energy.

It has been shown that the spin—orbit coupling (SOC) effect influences the band structure of perovskite materials significantly. To get a more accurate description of electronic structures, we perform single point energy calculations using PBE+SOC and HSE06⁵³ based on optimized geometries obtained from PBE calculations. The band gaps of pristine and defective CsPbI₂Br (100) slabs by PBE, PBE+SOC, and HSE06 are shown in Figure S3. The band gaps obtained using PBE fall between those calculated by using PBE+SOC and HSE06. The pristine CsPbI₂Br PBE calculation yields a band gap value of 1.91 eV, which agrees with the experimental value of 1.92 eV. Considering the low computational cost of PBE, its agreement with experimental values, and the reliability of optoelectronic properties for CsPbX₃ (X = Br, I) crystals, 78,79

all subsequent results presented in this study are calculated using PBE.

Figure 2 displays the density of states (DOS) of the pristine and defected surfaces. Around the band gap, the contribution is from Br, I, and Pb orbitals. The conduction band minimum (CBM) is mainly from Pb, with negligible contributions from Br and I, whereas the valence band maximum (VBM) is mainly from I. Figure S4 shows the energy band structures of the pristine and defective systems. All three studied defects introduce midgap states. V_I introduces a shallow defect state near the CBM. I_i introduces two shallow defect states near the VBM and a deep defect state located 0.8 eV above the VBM. Pb₁ introduces two shallow defect states near the CBM and a deep defect state around 0.9 eV below the CBM. It is generally assumed that the deep defect states located within the middle one-third of the bandgap.80 The formation of the deep defect states arises from strong interactions between the defective atom and its neighboring identical atoms, such as Pb-Pb and I-I. V_I can be considered as n-type defects. I_i shows both p-type and neutral character, while Pb_I shows both n-type and neutral character.

To further understand the effect of defects on the optical properties, we compute the absorption spectra (Equations S1–S2, Figure S5) for the pristine and defective systems, as shown in Figure 3. The pristine and $I_{\rm i}$ slabs have minimal absorbance below 1 eV, whereas slabs with Pb_I and V_I defects show light absorbance in this region. In the visible region, the pristine slab shows a stronger absorption of light than slabs with defects. In the ultraviolet region, both the pristine slab and the slab with $I_{\rm i}$ defect exhibit similar spectral signatures, displaying stronger absorption than slabs with Pb_I and V_I defects.

Figure 4 shows the partial charge densities of the VBM, CBM, and representative defect orbitals (shallow defect state orbital of V_I and deep defect state orbitals of I_i and Pb_I) for the pristine and defective systems. In the pristine system, the VBM is mainly distributed on the I atoms on the surface, and the

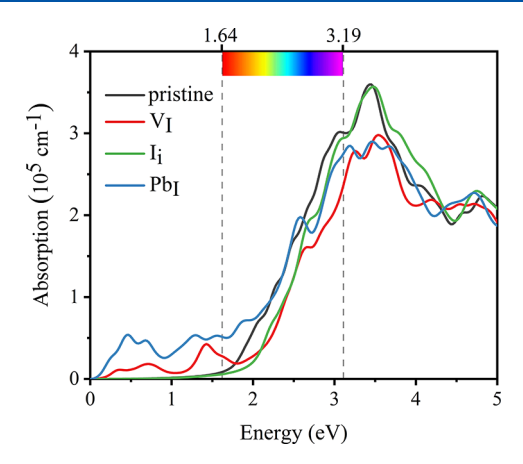


Figure 3. Calculated absorption spectra for pristine and defective CsPbI₂Br (100) surfaces. 1.64–3.19 eV is the energy absorption range for visible light.

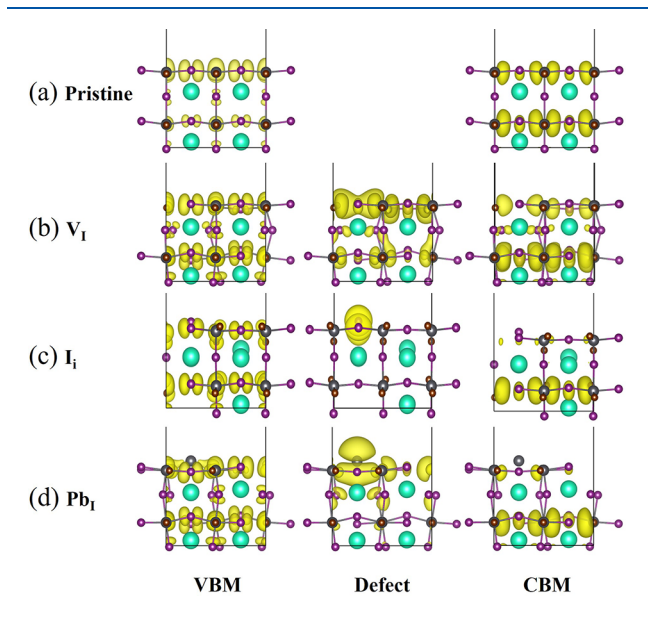


Figure 4. Partial charge densities in pristine and defective systems, including VBM, CBM, and defect states, for typical configurations at 0 K. The green, gray, brown, and purple spheres represent Cs, Pb, Br, and I atoms, respectively. The yellow surface represents partial charge density, and the red dashed circles indicate the locations of the defects.

CBM is mainly distributed on the Pb atoms, consistent with the DOS in Figure 2. V_I and Pb_I defects have a minor effect on the charge density of the CBM and VBM. For the I_i defect, the charge density of the VBM is depleted at the interstitial site, while the charge density is primarily localized at the interstitial site for the defect state. The charge density of the CBM is predominantly localized at the Pb atoms on the subsurface. The defective I atom on the surface has strong interactions with the surrounding I atoms, leading to I-p and I-p orbital coupling and thus the formation of an iodine trimer. 81,82 This charge redistribution may significantly reduce the NAC and thus suppress the e-h recombination rate.

The e-p interactions can significantly affect the electronic structures. Figure S6 depicts the time evolution of orbital energies for VBM, CBM, and representative defect states at 300 K. The fluctuations of the defect states along the MD trajectories are more pronounced compared to the VBM and

CBM, indicating that there is substantial e–p coupling in these impurity states. The slab with the $V_{\rm I}$ defect exhibits a shallow defect state close to the CBM, which shows slight oscillations with time (Figure S6b). The defect state for the slab with the $I_{\rm i}$ defect is close to the VBM and exhibits more substantial oscillations (Figure S6c), due to strong vibration of the foreign I atom. The defect state for the slab with the Pb_I defect also exhibits substantial oscillations (Figure S6d). The Pb atom occupies the site of the I atom, leading to strong p–p interactions between the defective Pb atom and neighboring Pb atoms.

To further investigate the effect of defects on the lifetime of excited-state carriers, we simulate e—h recombination and carrier relaxation for both pristine and defective structures through NAMD simulations. Thermal motion of atoms drives fluctuations of the electronic energy levels, and the fluctuations reflect the strength of elastic and inelastic electron—vibrational interactions that, respectively, induce coherence loss and are responsible for nonadiabatic transitions between electronic states.

Figure S7a shows the pure dephasing function obtained by the second-order cumulative approximation and with a Gaussian distribution $(\exp[-0.5(t/\tau)^2])$ to estimate the quantum coherence time as the pure dephasing time (τ) of the optical response theory as shown in Table 2. The V_I defect

Table 2. NACs, Pure Dephasing Times, and Recombination Times for the Pristine and Defective Systems

	NAC (meV)	Dephasing (fs)	Recombination (ns)
Pristine	0.555	4.268	89.82
$V_{\rm I}$	1.050	4.538	57.76
I_{i}	0.298	3.022	256.3
Pb_{I}	0.318	4.480	91.87

exhibits slower pure dephasing, because the corresponding energy gap and its fluctuations are minimal. The pure dephasing function decays most quickly for I_i , which has the most notable oscillations. The Pb_I defect exhibits comparable results to the pristine slab.

The e-p coupling affects NAC, leading to nonradiative relaxation of electrons and holes following optical excitation. To determine the time scale τ for nonradiative e-h recombination, we collect 1 ns NAMD data and fit exponential curves $(y(t) = \exp(-t/\tau))$ to the data points⁴⁶ (Table 2). Figure S7b depicts the evolution of the excited state populations of the pristine and defective systems due to nonradiative transitions. Various defects exhibit different recombination rates due to different initial values of the unnormalized autocorrelation function (Figure S8), pure dephasing time, and NACs (Figure S9).

The e-h recombination is often slowed by a greater band gap, a shorter pure-dephasing period, and a weaker NAC. Compared to the pristine slab, the formation of V_I speeds up e-h recombination, as it breaks bonds in the Pb-I lattice supporting the carriers and reduces the bandgap by introducing shallow energy levels below the CBM. Pb_I slightly accelerates the recombination. This is due to the formation of a localized midgap trap state between the defected Pb and the neighboring Pb, which is strongly coupled to the edge of VB. However, creating I_i increases the lifetime of the carriers. This is attributed to the formation of iodine trimers. The strong covalency introduces localized deep defect states with weak

couplings to the frontier orbitals. The slower charge recombination reduces energy dissipation into heat and improves the photon-to-electron conversion efficiency.

We calculate the hot electron relaxation dynamics from the CB edge states to the CBM and the hot hole relaxation dynamics from the VB edge states to the VBM, as shown in Figure S10. The relaxation times obtained by exponential fitting are listed in Table 3. We consider the average relaxation

Table 3. Relaxation Times of Hot Electrons and Hot Holes for the Pristine and Defective Systems

	Pristine	$V_{\rm I}$	I_i	Pb_{I}
Hot electron (fs)	402	454	590	605
Hot hole (fs)	397	305	152	230

effects from CBM+1, CBM+2, and CBM+3 to CBM and from VBM-1, VBM-2 and VBM-3 to VBM. All defects accelerate the relaxation of holes and slow down the relaxation of electrons. The formation of the I_i defect leads to a significant decrease in the relaxation time of hot holes. This is because the introduction of shallow defect states near the VBM reduces the energy level difference at the VB edge. The longer relaxation time of hot electrons implies that, during the cooling process, hot electrons can store more energy compared to hot holes. Therefore, it is expected that extracting hot electrons can maximize the utilization of solar energy and enhance the PCE of the perovskite.

A comparative analysis is conducted on the hot carrier relaxation dynamics in the pristine slab using two theoretical frameworks, namely, surface hopping and Redfield theories. As depicted in Figure 5, the computational results from both methodologies exhibit an analogous trend. For high-energy excitations, both approaches show increasing relaxation times with higher excitation energies, in agreement with the predictions of the energy gap law. 86 The excess energy acquired by hot carriers from higher-energy excitations leads to a greater accumulation of nonequilibrium longitudinal optical phonons.⁸⁷ Due to the hot-phonon effect, ^{88–90} which intensifies the interactions between electrons and phonons, the process of energy relaxation is slowed. This effect occurs because the hot carriers can reabsorb phonons before these phonons effectively dissipate their energies into the material's lattice. Consequently, hot carriers require additional time to

release their excess energies and reach thermal equilibrium with the lattice, which acts as a thermal reservoir. At lower excitation energies, the relaxation times obtained from both methods deviates from the linear trend. It is found that the relaxation times increase with decreasing excitation energies. This is attributed to the scarcity of energy relaxation pathways available near the band edges in the material. 91 At lower initial excitation energies, the strong coupling near the bandgap edge facilitates the formation of polarons by trapping the generated hot electrons, resulting in slower relaxation rates. This is one of the important reasons perovskite materials exhibit long carrier lifetimes. As the excitation energy continues to increase, the influence of phonons destabilizes the polarons, thereby accelerating the relaxation rates of the hot carriers. This acceleration persists until the emergence of the hot-phonon bottleneck, at which point the relaxation rates slow down with increasing excitation energies. Notably, the relaxation rates of holes, as determined by both methods, surpass that of electrons, a phenomenon attributed to the higher density of states in the VB compared to the CB. 92 Under the same initial excitation energy, the number of bands in the CB is fewer than those in the VB. In certain scenarios, the subgaps in the CB are greater than that in the VB. Consequently, hot electrons in the CB undergo interband relaxation through band-to-band fluctuations. In contrast, hot holes in the VB, due to the smaller energy gap, can directly relax between bands. Simultaneously, the lower band density enhances the hotphonon effect, thereby further decelerating the relaxation process of the hot electrons.

We choose suitable excitation energies to further investigate and compare the relaxation behavior of both methods. Figure 6a–c depicts the nonradiative relaxation dynamics of charge carriers for initial orbitals CBM+10 and VBM-20 in the pristine system obtained by the surface hopping and Redfield methods. Figure 6d,e, along with Tables S2 and S3, present the relaxation times of hot carriers in the defective and pristine systems for both methods, based on the selected energy level differences (ΔE_e and ΔE_h). Although there are numerical discrepancies in the relaxation times obtained by the two methods, a consistent trend is observed. Compared to the surface hopping method, the Redfield method yields longer relaxation times for both electrons and holes, with the difference being more pronounced for electrons than for holes. The surface hopping method primarily accounts for

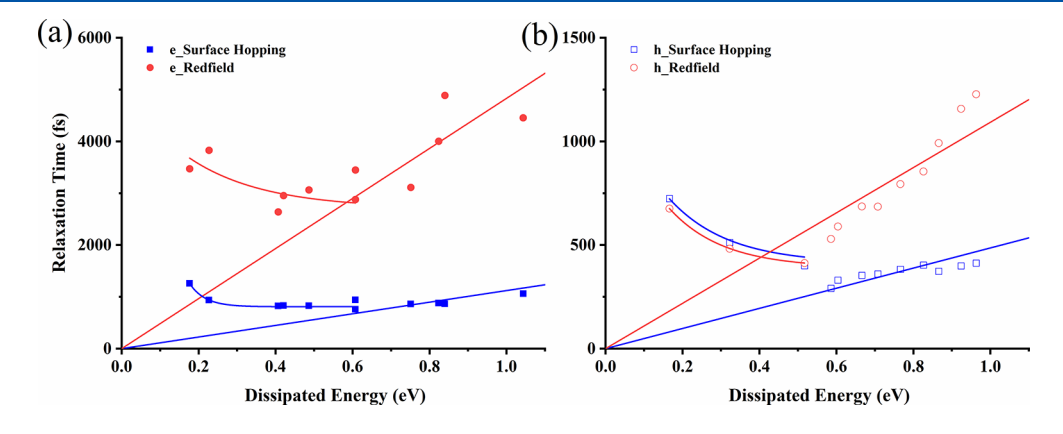


Figure 5. Relaxation times in the pristine slab for (a) hot electron and (b) hot hole cooling under various initial excitation states, with the x-axis representing the energy level differences ($E_{CBM+i}-E_{CBM}$ for the conduction band and $E_{VBM}-E_{VBM-i}$ for the valence band) and the y-axis denoting the relaxation times. The blue and red colors correspond to results from surface hopping and Redfield methods, respectively.

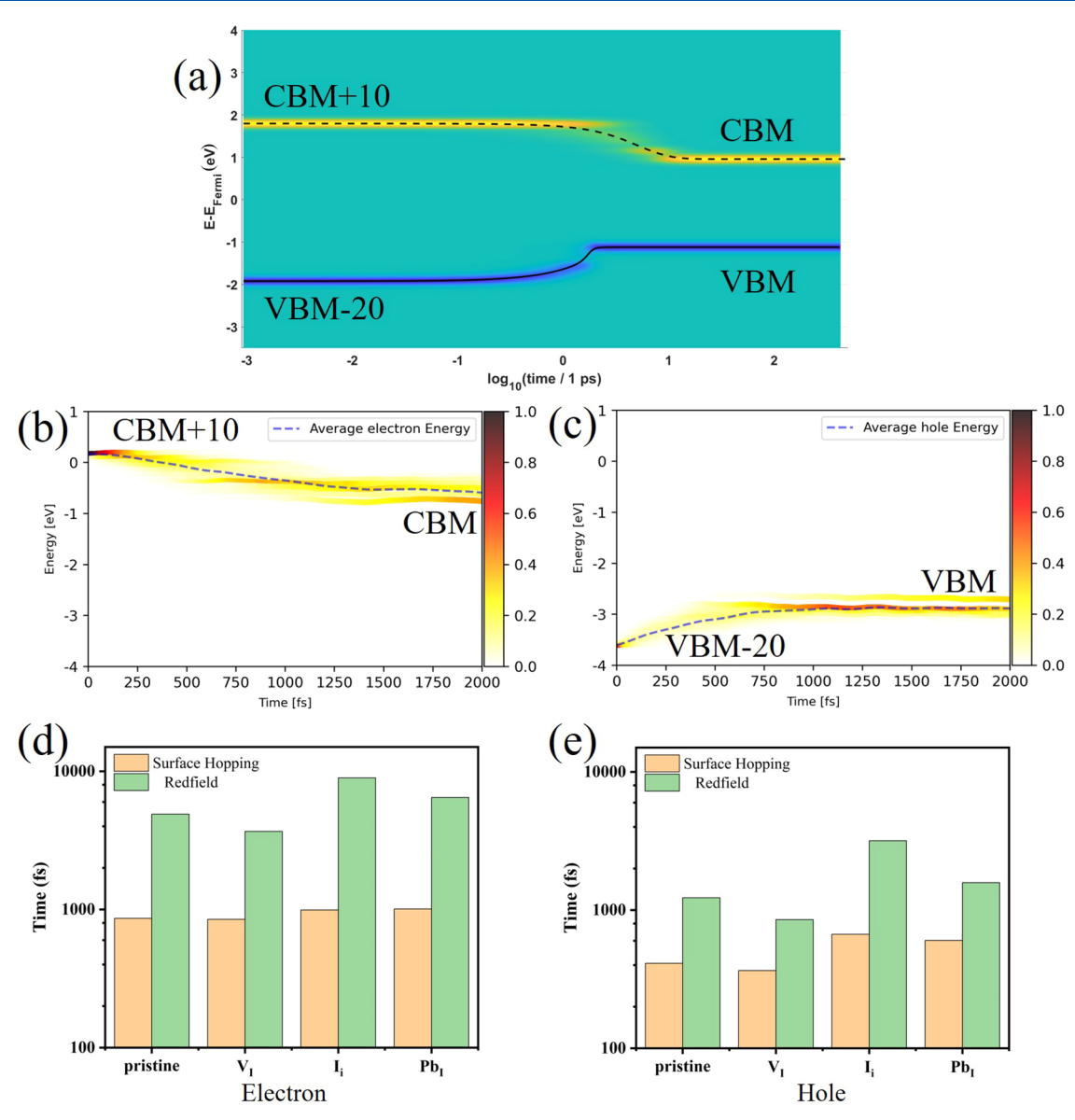


Figure 6. (a-c) Nonradiative relaxation dynamics of charge carriers for the initial orbitals CBM+10 and VBM-20 in the pristine system. (a) The relaxation is obtained by the Redfield method. The yellow (blue) lines depict the nonequilibrium charge density of the photoexcited electron (hole), and the dotted (solid) line represents the average energy of the electron (hole). (b and c) The energy relaxation processes of electrons and holes obtained by the surface hopping method, respectively. The ribbons denote the distribution of electrons and holes among different states, while the dashed lines indicate the average electron and hole energies. (d) and (e) present the electron and hole relaxation times obtained by the two methods in both the pristine and defective slabs. Their initial energy levels are different, and Tables S3 and S4 provide the relevant initial energy levels.

instantaneous/random hops between potential energy surfaces while explicitly monitoring dependence of subgaps on time in molecular systems, while the Redfield theory primarily considers an average relaxation induced by the interaction between electronic and nuclear degrees of freedom, representing the environment. While both methods are based on the same protocol of computing nonadiabatic couplings, surface hopping and Redfield approaches perform an averaging procedure over an ensemble of nuclear motion at different stages. Specifically, the surface hopping algorithm does electronic transitions first, averaging second, while the Redfield approach does average first, electronic transitions second.

Both methods exhibit consistency in the influence of various defects on the relaxation process. The presence of $V_{\rm I}$ defects accelerates the relaxation of both electrons and holes, while the

presence of I_i and Pb_I defects decelerates the relaxation of both electrons and holes. Additionally, the electron relaxation times obtained by both methods are longer than the hole relaxation times. The ratios of defect-induced electron and hole relaxation rates relative to the pristine counterparts are depicted in Figure S11a,b and summarized in Tables S4 and S5. The relative rate changes obtained from the Hefei-NAMD program exhibit variations between 1-2 times, while those from the Redfield theory range from 1-3 times.

In summary, we have investigated the effects of the intrinsic surface defects (V_D, I_i) and $Pb_I)$ on the geometrical and optoelectronic properties of $CsPbI_2Br$ perovskites using first-principles calculations as well as their charge carrier recombination and relaxation dynamics processes using NAMD simulations. All studied surface defects have slight

effects on visible light absorption. However, surfaces with V_I and Pb_I defects exhibit enhanced absorbance in the nearinfrared region, indicating that the presence of defects may expand the light absorption region and increase the generated photocurrent. The formation of V_I defects introduces shallow defect states and accelerates the e-h recombination rate. This is because vacancy defects make electrons more delocalized and enhance nuclear motion in the perturbed lattice, resulting in larger NACs. The formation of Pb_I defects creates deep defect states and accelerates the e-h recombination, whereas the formation of Ii defects slows down the carrier recombination. The lattice deformation caused by I_i defects reduces the overlap between the defect states and frontier orbitals through covalent bonds in the iodine trimer. A more in-depth investigation into the impact of defects on the relaxation of hot charge carriers is conducted through a comparative study between surface hopping and Redfield methods. Although there are numerical discrepancies in the relaxation times obtained by the two methods, a consistent trend is observed. Both methods reveal that V_I defects accelerate the relaxation process, while Ii and PbI defects decelerate the relaxation process. The temporal differences between the two methods stem from the distinct factors considered and the various approximations employed. Our discovery highlights a crucial design principle for all-inorganic mixed-halide perovskite materials utilized in numerous photovoltaic applications: a synthesis environment rich in I favors the formation of I interstitial defects and reduces the occurrence of vacancy defects, which further slows carrier recombination and thereby enhances PCE.

ASSOCIATED CONTENT

Supporting Information

The Supporting Information is available free of charge at https://pubs.acs.org/doi/10.1021/acs.jpclett.4c00675.

Computational methods; optimized four different terminations of the CsPbI₂Br(100) surface; defect formation energies of different defects on the CsPbI₂Br surface; band gaps of CsPbI₂Br (100) surface calculated by PBE, PBE + SOC, and HSE06; energy band structure of pristine and defective (V_I, I_i, and Pb_I) CsPbI₂Br (100) surface with PBE; the imaginary part of the dielectric function for the pristine CsPbI2Br system; evolution of orbital energies for VBM, CBM, and defect levels with time in the CsPbI₂Br system at 300 K; pure dephasing function of the VBM-CBM jump in the CsPbI₂Br system obtained by Hefei-NAMD; charge recombination processes of pristine and defective CsPbI2Br; calculated unnormalized autocorrelation functions and spectral densities of the pristine and defect-bearing CsPbI₂Br perovskites; calculated nonadiabatic coupling matrices of the pristine and defect-bearing CsPbI₂Br perovskites; average hot electron relaxation processes of defective and defect-free CsPbI₂Br from CBM+1, CBM +2, and CBM+3 to CBM; average hot hole relaxation processes of defective and defect-free CsPbI2Br from VBM-1, VBM-2, and VBM-3 to VBM; the rate of electrons and holes of the defective system relative to the pristine system obtained by the two methods; stoichiometry of studied models; the relaxation times of electrons obtained by the two methods for the selected initial energy levels; relaxation times of holes

obtained by the two methods for the selected initial energy levels; and the rates of electrons for the defective system relative to the pristine system obtained by both methods for the chosen initial energy level (PDF)

AUTHOR INFORMATION

Corresponding Authors

Shuping Huang — College of Chemistry, Fuzhou University, Fuzhou, Fujian 350108, P. R. China; State Key Laboratory of Structural Chemistry, Fujian Institute of Research on the Structure of Matter, Chinese Academy of Sciences, Fuzhou 350002, P. R. China; orcid.org/0000-0003-4815-1863; Email: huangshp@fzu.edu.cn

Yulun Han — Department of Chemistry and Biochemistry, North Dakota State University, Fargo, North Dakota 58108, United States; orcid.org/0000-0002-8619-0233; Email: yulun.han@ndsu.edu

Dmitri S. Kilin — Department of Chemistry and Biochemistry, North Dakota State University, Fargo, North Dakota 58108, United States; orcid.org/0000-0001-7847-5549; Email: dmitri.kilin@ndsu.edu

Authors

Bao Liu — College of Chemistry, Fuzhou University, Fuzhou, Fujian 350108, P. R. China

Zhaoxin Wang - College of Chemistry, Fuzhou University, Fuzhou, Fujian 350108, P. R. China

Complete contact information is available at: https://pubs.acs.org/10.1021/acs.jpclett.4c00675

Notes

The authors declare no competing financial interest.

■ ACKNOWLEDGMENTS

S.H. acknowledges financial supports from the National Natural Science Foundation of China (21703036) and the Natural Science Foundation of Fujian Province (2021J01547). D.K. and Y.H. acknowledge support of NSF 1944921 for methods development.

REFERENCES

- (1) Ma, Y.; Gong, J.; Zeng, P.; Liu, M. Recent Progress in Interfacial Dipole Engineering for Perovskite Solar Cells. *Nano-micro lett.* **2023**, 15, 173–173.
- (2) Wang, Y.; Zhang, Y.; Zhang, P.; Zhang, W. High Intrinsic Carrier Mobility and Photon Absorption in the Perovskite CH₃NH₃PbI₃. *Phys. Chem. Chem. Phys.* **2015**, *17*, 11516–11520.
- (3) Xing, G.; Mathews, N.; Sun, S.; Lim, S. S.; Lam, Y. M.; Graetzel, M.; Mhaisalkar, S.; Sum, T. C. Long-Range Balanced Electron- and Hole-Transport Lengths in Organic-Inorganic CH₃NH₃PbI₃. *Science* **2013**, 342, 344–347.
- (4) Hodes, G. Perovskite-Based Solar Cells. Science 2013, 342, 317–318.
- (5) Zhang, L.; Mei, L.; Wang, K.; Lv, Y.; Zhang, S.; Lian, Y.; Liu, X.; Ma, Z.; Xiao, G.; Liu, Q. Advances in the Application of Perovskite Materials. *Nano-micro lett.* **2023**, *15*, 177.
- (6) Yuan, H.; Zhao, Y.; Duan, J.; Wang, Y.; Yang, X.; Tang, Q. Allinorganic CsPbBr₃ Perovskite Solar Cell with 10.26% Efficiency by Spectra Engineering. *J. Mater. Chem. A* **2018**, *6*, 24324–24329.
- (7) Li, B.; Zhang, Y.; Fu, L.; Yu, T.; Zhou, S.; Zhang, L.; Yin, L. Surface Passivation Engineering Strategy to Fully-Inorganic Cubic CsPbI₃ Perovskites for High-Performance Solar Cells. *Nat. Commun.* **2018**, *9*, 1076.

- (8) Sun, J.-K.; Huang, S.; Liu, X.-Z.; Xu, Q.; Zhang, Q.-H.; Jiang, W.-J.; Xue, D.-J.; Xu, J.-C.; Ma, J.-Y.; Ding, J.; et al. Polar Solvent Induced Lattice Distortion of Cubic CsPbI₃ Nanocubes and Hierarchical Self-Assembly into Orthorhombic Single-Crystalline Nanowires. *J. Am. Chem. Soc.* **2018**, *140*, 11705–11715.
- (9) Kulbak, M.; Cahen, D.; Hodes, G. How Important Is the Organic Part of Lead Halide Perovskite Photovoltaic Cells? Efficient CsPbBr₃ Cells. *J. Phys. Chem. Lett.* **2015**, *6*, 2452–2456.
- (10) Chang, S.; Bai, Z.; Zhong, H. In Situ Fabricated Perovskite Nanocrystals: A Revolution in Optical Materials. *Adv. Opt. Mater.* **2018**, *6*, No. 1800380.
- (11) Kang, J.; Wang, L.-W. High Defect Tolerance in Lead Halide Perovskite CsPbBr₃. J. Phys. Chem. Lett. 2017, 8, 489–493.
- (12) Stoumpos, C. C.; Malliakas, C. D.; Peters, J. A.; Liu, Z.; Sebastian, M.; Im, J.; Chasapis, T. C.; Wibowo, A. C.; Chung, D. Y.; Freeman, A. J.; et al. Crystal Growth of the Perovskite Semiconductor CsPbBr₃: A New Material for High-Energy Radiation Detection. *Cryst. Growth Des.* **2013**, *13*, 2722–2727.
- (13) Sanchez, S.; Christoph, N.; Grobety, B.; Phung, N.; Steiner, U.; Saliba, M.; Abate, A. Efficient and Stable Inorganic Perovskite Solar Cells Manufactured by Pulsed Flash Infrared Annealing. *Adv. Energy Mater.* **2018**, *8*, No. 1802060.
- (14) Xiang, W.; Tress, W. Review on Recent Progress of All-Inorganic Metal Halide Perovskites and Solar Cells. *Adv. Mater.* **2019**, *31*, No. 1902851.
- (15) Ho-Baillie, A.; Zhang, M.; Lau, C. F. J.; Ma, F.-J.; Huang, S. Untapped Potentials of Inorganic Metal Halide Perovskite Solar Cells. *Joule* **2019**, *3*, 938–955.
- (16) Song, J.; Xie, H.; Lim, E. L.; Hagfeldt, A.; Bi, D. Progress and Perspective on Inorganic CsPbI₂Br Perovskite Solar Cells. *Adv. Energy Mater.* **2022**, *12*, No. 2201854.
- (17) Liu, X.; Li, J.; Cui, X.; Wang, X.; Yang, D. The Progress and Efficiency of CsPbI₂Br Perovskite Solar Cells. *J. Mater. Chem. C* **2023**, 11, 426–455.
- (18) Lim, E. L.; Yang, J.; Wei, Z. Inorganic CsPbI₂Br Halide Perovskites: From Fundamentals to Solar Cell Optimizations. *Energy Environ. Sci.* **2023**, *16*, 862–888.
- (19) Ding, Y.; Guo, Q.; Geng, Y.; Dai, Z.; Wang, Z.; Chen, Z.; Guo, Q.; Zheng, Z.; Li, Y.; Zhou, E. A Low-Cost Hole Transport Layer Enables CsPbI₂Br Single-Junction and Tandem Perovskite Solar Cells with Record Efficiencies of 17.8% and 21.4%. *Nano Today* **2022**, 46, No. 101586.
- (20) Jiang, X.; Zang, Z.; Zhou, Y.; Li, H.; Wei, Q.; Ning, Z. Tin Halide Perovskite Solar Cells: An Emerging Thin-Film Photovoltaic Technology. *Acc. Chem. Res.* **2021**, *2*, 210–219.
- (21) Stolterfoht, M.; Wolff, C. M.; Marquez, J. A.; Zhang, S.; Hages, C. J.; Rothhardt, D.; Albrecht, S.; Burn, P. L.; Meredith, P.; Unold, T.; et al. Visualization and Suppression of Interfacial Recombination for High-efficiency Large-area pin Perovskite Solar Cells. *Nat. Energy* **2018**, *3*, 847–854.
- (22) Schulz, P. Interface Design for Metal Halide Perovskite Solar Cells. ACS Energy Lett. 2018, 3, 1287–1293.
- (23) Han, Y.; Zhao, H.; Duan, C.; Yang, S.; Yang, Z.; Liu, Z.; Liu, S. Controlled n-Doping in Air-Stable CsPbI2Br Perovskite Solar Cells with a Record Efficiency of 16.79%. *Adv. Funct. Mater.* **2020**, *30*, No. 1909972.
- (24) Gong, X.; Guan, L.; Li, Q.; Li, Y.; Zhang, T.; Pan, H.; Sun, Q.; Shen, Y.; Graetzel, C.; Zakeeruddin, S. M.; et al. Black Phosphorus Quantum Dots in Inorganic Perovskite thin Films for Efficient Photovoltaic Application. *Sci. Adv.* **2020**, *6*, 406.
- (25) Byranvand, M. M.; Saliba, M. Defect Passivation of Perovskite Films for Highly Efficient and Stable Solar Cells. *Sol. RRL* **2021**, *5*, No. 2100295.
- (26) Peng, J.; Wu, Y.; Ye, W.; Jacobs, D. A.; Shen, H.; Fu, X.; Wan, Y.; Duong, T.; Wu, N.; Barugkin, C.; et al. Interface Passivation using Ultrathin Polymer-Fullerene Films for High-efficiency Perovskite Solar Cells with Negligible Hysteresis. *Energy Environ. Sci.* **2017**, *10*, 1792–1800.

- (27) Ni, Z.; Bao, C.; Liu, Y.; Jiang, Q.; Wu, W.-Q.; Chen, S.; Dai, X.; Chen, B.; Hartweg, B.; Yu, Z.; et al. Resolving Spatial and Energetic Distributions of Trap States in Metal Halide Perovskite Solar Cells. *Science* **2020**, *367*, 1352–1358.
- (28) Tan, H.; Jain, A.; Voznyy, O.; Lan, X.; García de Arquer, F. P. G.; Fan, J. Z.; Quintero-Bermudez, R.; Yuan, M.; Zhang, B.; Zhao, Y.; et al. Efficient and Stable Solution-Processed Planar Perovskite Solar Cells via Contact Passivation. *Science* **2017**, *355*, 722–726.
- (29) Zheng, S.; Wang, G.; Liu, T.; Lou, L.; Xiao, S.; Yang, S. Materials and Structures for the Electron Transport Layer of Efficient and Stable Perovskite Solar Cells. *Sci. China: Chem.* **2019**, *62*, 800–800
- (30) Chen, X.; Cheng, J.; He, L.; Zhao, L.; Zhang, C.; Pang, A.; Li, J. Hole Transport Materials for Tin-Based Perovskite Solar Cells: Properties, Progress, Prospects. *Molecules* **2023**, *28*, 3787.
- (31) Ansari, M. I. H.; Qurashi, A.; Nazeeruddin, M. K. Frontiers, Opportunities, and Challenges in Perovskite Solar Cells: A Critical Review. *J. Photochem. Photobiol.*, C **2018**, 35, 1–24.
- (32) Jones, T. W.; Osherov, A.; Alsari, M.; Sponseller, M.; Duck, B. C.; Jung, Y.-K.; Settens, C.; Niroui, F.; Brenes, R.; Stan, C. V.; et al. Lattice Strain Causes Non-radiative Losses in Halide Perovskites. *Energy Environ. Sci.* **2019**, *12*, 596–606.
- (33) Xia, J.; Zhang, Y.; Xiao, C.; Brooks, K. G.; Chen, M.; Luo, J.; Yang, H.; Klipfel, N. I. D.; Zou, J.; Shi, Y.; et al. Tailoring Electric Dipole of Hole-Transporting Material P-dopants for Perovskite Solar Cells. *Joule* **2022**, *6*, 1689–1709.
- (34) Xiao, Z.; Yuan, Y.; Shao, Y.; Wang, Q.; Dong, Q.; Bi, C.; Sharma, P.; Gruverman, A.; Huang, J. Giant Switchable Photovoltaic Effect in Organometal Trihalide Perovskite Devices. *Nat. Mater.* **2015**, *14*, 193–198.
- (35) Ran, C.; Xu, J.; Gao, W.; Huang, C.; Dou, S. Defects in Metal Triiodide Perovskite Materials Towards High-Performance Solar Cells: Origin, Impact, Characterization, and Engineering. *Chem. Soc. Rev.* **2018**, *47*, 4581–4610.
- (36) Wang, F.; Bai, S.; Tress, W.; Hagfeldt, A.; Gao, F. Defects Engineering for High-Performance Perovskite Solar Cells. *Npj Flexible Electron.* **2018**, *2*, 22.
- (37) Wang, B.; Yin, X.; Iqbal, S.; Que, M.; Que, W. Recent Progress on Defect Passivation of All-Inorganic Halide Perovskite Solar Cells. *Adv. Mater. Interfaces* **2022**, *9*, No. 2200636.
- (38) Isikgor, F. H.; Zhumagali, S.; Merino, L. V. T.; De Bastiani, M.; McCulloch, I.; De Wolf, S. Molecular Engineering of Contact Interfaces for High-Performance Perovskite Solar Cells. *Nat. Rev. Mater.* **2023**, *8*, 89–108.
- (39) Liu, Z.; Chen, Q.; Lee, J.-W.; Zhao, Z.; Xu, X.; Hsieh, Y.-T.; Meng, L.; Sun, P.; De Marco, N.; Zhou, H.; et al. Rationally Induced Interfacial Dipole in Planar Heterojunction Perovskite Solar Cells for Reduced J-V Hysteresis. *Adv. Energy Mater.* **2018**, *8*, No. 1800568.
- (40) Weber, S. A. L.; Hermes, I. M.; Turren-Cruz, S.-H.; Gort, C.; Bergmann, V. W.; Gilson, L.; Hagfeldt, A.; Graetzel, M.; Tress, W.; Berger, R. How the Formation of Interfacial Charge Causes Hysteresis in Perovskite Solar Cells. *Energy Environ. Sci.* **2018**, *11*, 2404–2413.
- (41) Kawano, K.; Adachi, C. Evaluating Carrier Accumulation in Degraded Bulk Heterojunction Organic Solar Cells by a Thermally Stimulated Current Technique. *Adv. Funct. Mater.* **2009**, *19*, 3934–3940.
- (42) Choi, K.; Lee, J.; Kim, H. I.; Park, C. W.; Kim, G.-W.; Choi, H.; Park, S.; Park, S. A.; Park, T. Thermally Stable, Planar Hybrid Perovskite Solar Cells with High Efficiency. *Energy Environ. Sci.* **2018**, *11*, 3238–3247.
- (43) Xia, J.; Sohail, M.; Nazeeruddin, M. K. Efficient and Stable Perovskite Solar Cells by Tailoring of Interfaces. *Adv. Mater.* **2023**, *35*, No. 2211324.
- (44) Zheng, Z.; Shi, Y.; Zhou, J.-J.; Prezhdo, O. V.; Zheng, Q.; Zhao, J. Ab initio real-time quantum dynamics of charge carriers in momentum space. *Nat. Comput. Sci.* **2023**, *3*, 532–541.
- (45) Chu, W. B.; Zheng, Q. J.; Akimov, A. V.; Zhao, J.; Saidi, W. A.; Prezhdo, O. V. Accurate Computation of Nonadiabatic Coupling with

- Projector Augmented-Wave Pseudopotentials. J. Phys. Chem. Lett. 2020, 11, 10073-10080.
- (46) Chu, W. B.; Saidi, W. A.; Zhao, J.; Prezhdo, O. V. Soft Lattice and Defect Covalency Rationalize Tolerance of β -CsPbI₃ Perovskite Solar Cells to Native Defects. *Angew. Chem., Int. Ed.* **2020**, *59*, 6435–6441.
- (47) Nayakasinghe, M. T.; Han, Y.; Sivapragasam, N.; Kilin, D. S.; Oncel, N.; Burghaus, U. Adsorption of Formic Acid on CH₃NH₃PbI₃ Lead-Halide Organic-Inorganic Perovskites. *J. Phys. Chem. C* **2019**, 123, 22873–22886.
- (48) Nayakasinghe, M. T.; Han, Y.; Sivapragasam, N.; Kilin, D. S.; Burghaus, U. Unexpected high binding energy of CO₂ on CH₃NH₃PbI₃ lead-halide organic-inorganic perovskites via bicarbonate formation. *Chem. Commun.* **2018**, *54*, 9949–9952.
- (49) Johnson, L.; Kilin, D. Effect of ligand groups on photoexcited charge carrier dynamics at the perovskite/TiO₂ interface. *Rsc Advances* **2021**, *12*, 78–87.
- (50) Graupner, D. R.; Kilin, D. S. Size effects on polaron formation in lead chloride perovskite thin films. *Mol. Phys.* **2023**, DOI: 10.1080/00268976.2023.2273418.
- (51) Huang, S.; Kilin, D. S. Charge Transfer, Luminescence, and Phonon Bottleneck in ${\rm TiO_2}$ Nanowires Computed by Eigenvectors of Liouville Superoperator. *J. Chem. Theory Comput.* **2014**, *10*, 3996–4005.
- (52) Meng, X.; Wang, Z.; Qian, W.; Zhu, Z.; Zhang, T.; Bai, Y.; Hu, C.; Xiao, S.; Yang, Y.; Yang, S. Excess Cesium Iodide Induces Spinodal Decomposition of CsPbI₂Br Perovskite Films. *J. Phys. Chem. Lett.* **2019**, *10*, 194–199.
- (53) Chen, Y.; Shi, T.; Liu, P.; Xie, W.; Chen, K.; Xu, X.; Shui, L.; Shang, C.; Chen, Z.; Yip, H.-L.; et al. The distinctive phase stability and defect physics in CsPbI₂Br perovskite. *J. Mater. Chem. A* **2019**, 7, 20201–20207.
- (54) Sutton, R. J.; Eperon, G. E.; Miranda, L.; Parrott, E. S.; Kamino, B. A.; Patel, J. B.; Horantner, M. T.; Johnston, M. B.; Haghighirad, A. A.; Moore, D. T.; et al. Bandgap-Tunable Cesium Lead Halide Perovskites with High Thermal Stability for Efficient Solar Cells. *Adv. Energy Mater.* **2016**, *6*, No. 1502458.
- (55) Wang, H.; Zhang, X.; Wu, Q.; Cao, F.; Yang, D.; Shang, Y.; Ning, Z.; Zhang, W.; Zheng, W.; Yan, Y.; et al. Trifluoroacetate Induced Small-Grained CsPbBr₃ Perovskite Films Result in Efficient and Stable Light-Emitting Devices. *Nat. Commun.* **2019**, *10*, 665.
- (56) Dong, Y.; Guo, Y.; Wang, M.; Zhu, R.; Ma, D.; Jia, Y. Designing Multifunctional Donor-Acceptor-Type Molecules to Passivate Surface Defects Efficiently and Enhance Charge Transfer of CsPbI₂Br Perovskite for High Power Conversion Efficiency. *Inorg. Chem.* **2022**, *61*, 9469–9479.
- (57) Kresse, G.; Furthmuller, J. Efficiency of Ab-initio Total Energy Calculations for Metals and Semiconductors using a Plane-wave Basis Set. *Comput. Mater. Sci.* **1996**, *6*, 15–50.
- (58) Kresse, G.; Furthmuller, J. Efficient Iterative Schemes for Ab Initio Total-energy Calculations using a Plane-wave Basis Set. *Phys. Rev. B* **1996**, *54*, 11169–11186.
- (59) Perdew, J. P.; Burke, K.; Ernzerhof, M. Generalized Gradient Approximation Made Simple. *Phys. Rev. Lett.* **1996**, 77, 3865–3868.
- (60) Blochl, P. E. Projector Augmeted-wave Method. *Phys. Rev. B* **1994**, *50*, 17953–17979.
- (61) Uratani, H.; Yamashita, K. Charge Carrier Trapping at Surface Defects of Perovskite Solar Cell Absorbers: A First-Principles Study. *J. Phys. Chem. Lett.* **2017**, *8*, 742–746.
- (62) Akimov, A. V.; Prezhdo, O. V. The PYXAID Program for Non-Adiabatic Molecular Dynamics in Condensed Matter Systems. *J. Chem. Theory Comput.* **2013**, *9*, 4959–4972.
- (63) Akimov, A. V.; Prezhdo, O. V. Advanced Capabilities of the PYXAID Program: Integration Schemes, Decoherencie Effects, Multiexcitonic States, and Field-Matter Interaction. *J. Chem. Theory Comput.* **2014**, *10*, 789–804.
- (64) Zheng, Q.; Saidi, W. A.; Xie, Y.; Lan, Z.; Prezhdo, O. V.; Petek, H.; Zhao, J. Phonon-Assisted Ultrafast Charge Transfer at van der Waals Heterostructure Interface. *Nano Lett.* **2017**, *17*, 6435–6442.

- (65) Chu, W.; Saidi, W. A.; Zheng, Q.; Xie, Y.; Lan, Z.; Prezhdo, O. V.; Petek, H.; Zhao, J. Ultrafast Dynamics of Photongenerated Holes at a CH₃OH/TiO₂ Rutile Interface. *J. Am. Chem. Soc.* **2017**, *139*, 10164–10164.
- (66) Zheng, Q.; Chu, W.; Zhao, C.; Zhang, L.; Wang, Y.; Guo, H.; Jiang, X.; Zhao, J. Ab Initio Nonadiabatic Molecular Dynamics Investigations on the Excited Carriers in Condensed Matter Systems. *Abstr. Pap. Am. Chem. Soc.* **2019**, *9*, No. e1411.
- (67) Zhang, L.; Zheng, Q.; Xie, Y.; Lan, Z.; Prezhdo, O. V.; Saidi, W. A.; Zhao, J. Delocalized Impurity Phonon Induced Electron-Hole Recombination in Doped Semiconductors. *Nano Lett.* **2018**, *18*, 1592–1599.
- (68) Tully, J. C. Molecular Dynamics with Electronic Transitions. *J. Chem. Phys.* **1990**, 93, 1061–1071.
- (69) Craig, C. F.; Duncan, W. R.; Prezhdo, O. V. Trajectory Surface Hopping in the Time-Dependent Kohn-Sham Approach for Electron-Nuclear Dynamics. *Phys. Rev. Lett.* **2005**, *95*, No. 163001.
- (70) Jean, J. M.; Friesner, R. A.; Fleming, G. R. Application of a multilevel Redfield theory to electron transfer in condensed phases. *J. Chem. Phys.* **1992**, *96*, 5827–5842.
- (71) Redfield, A. G. On the Theory of Relaxation Processes. *IBM J. Res. Dev.* **1957**, *1*, 19–31.
- (72) Tong, C.-J.; Li, L.; Liu, L.-M.; Prezhdo, O. V. Long Carrier Lifetimes in PbI₂-Rich Perovskites Rationalized by Ab Initio Nonadiabatic Molecular Dynamics. *ACS Energy Lett.* **2018**, *3*, 1868–1874.
- (73) Bi, D.; Tress, W.; Dar, M. I.; Gao, P.; Luo, J.; Renevier, C.; Schenk, K.; Abate, A.; Giordano, F.; Baena, J.-P. C.; et al. Efficient luminescent Solar Cells based on Tailored Mixed-Cation Perovskites. *Sci. Adv.* **2016**, *2*, No. e1501170.
- (74) Jacobsson, T. J.; Correa-Baena, J.-P.; Halvani Anaraki, E.; Philippe, B.; Stranks, S. D.; Bouduban, M. E. F.; Tress, W.; Schenk, K.; Teuscher, J.; Moser, J.-E.; et al. Unreacted PbI₂ as a Double-Edged Sword for Enhancing the Performance of Perovskite Solar Cells. *J. Am. Chem. Soc.* **2016**, *138*, 10331–10343.
- (75) Zhang, X.; Zhang, D.; Guo, T.; Zheng, C.; Zhou, Y.; Jin, J.; Zhu, Z.; Wang, Z.; Cui, X.; Wu, S.; et al. The Synergistic Effect of Defect Passivation and Energy level Adjustment for Low-temperature Carbon-based CsPbI₂Br Perovskite Solar Cells. *J. Mater. Chem. C* **2022**, *10*, 15573–15581.
- (76) Shan, W. T.; Saidi, W. A. Segregation of Native Defects to the Grain Boundaries in Methylammonium Lead Iodide Perovskite. *J. Phys. Chem. Lett.* **2017**, *8*, 5935–5942.
- (77) Li, W.; Zhou, L.; Prezhdo, O. V.; Akimov, A. V. Spin-Orbit Interactions Greatly Accelerate Nonradiative Dynamics in Lead Halide Perovskites. *ACS Energy Lett.* **2018**, *3*, 2159–2166.
- (78) Ghaithan, H. M.; Alahmed, Z. A.; Lyras, A.; Qaid, S. M. H.; Aldwayyan, A. S. Computational Investigation of the Folded and Unfolded Band Structure and Structural and Optical Properties of $CsPb(I_{1-x}Br_x)_3$ Perovskites. *Crystals* **2020**, *10*, 342.
- (79) Ghaithan, H. M.; Alahmed, Z. A.; Qaid, S. M. H.; Aldwayyan, A. S. Density Functional Theory Analysis of Structural, Electronic, and Optical Properties of Mixed-Halide Orthorhombic Inorganic Perovskites. *Acs Omega* **2021**, *6*, 30752–30761.
- (80) Chen, X.; Cheng, S.; Xiao, L.; Sun, H. Identifying, Understanding and Controlling Defects and Traps in Halide Perovskites for Optoelectronic Devices: a Review. *J. Phys. D: Appl. Phys.* **2020**, 53, No. 373001.
- (81) Agiorgousis, M. L.; Sun, Y.-Y.; Zeng, H.; Zhang, S. Strong Covalency-Induced Recombination Centers in Perovskite Solar Cell Material CH₃NH₃Pbl₃. *J. Am. Chem. Soc.* **2014**, *136*, 14570–14575.
- (82) Ruth, A.; Holland, M.; Rockett, A.; Sanehira, E.; Irwin, M. D.; Steirer, K. X. Charge Compensation by Iodine Covalent Bonding in Lead Iodide Perovskite Materials. *Crystals* **2022**, *12*, 88.
- (83) Chu, W.; Saidi, W. A.; Zhao, J.; Prezhdo, O. V. Soft Lattice and Defect Covalency Rationalize Tolerance of beta-CsPbI₃ Perovskite Solar Cells to Native Defects. *Angew. Chem., Int. Ed.* **2020**, *59*, 6435–6441.

- (84) Zhang, Z.; Qiao, L.; Mora-Perez, C.; Long, R.; Prezhdo, O. V. Pb Dimerization Greatly Accelerates Charge Losses in MAPbI(3): Time-Domain ab Initio Analysis. *J. Chem. Phys.* **2020**, *152*, No. 064707.
- (85) Zhou, Z.; He, J.; Frauenheim, T.; Prezhdo, O. V.; Wang, J. Control of Hot Carrier Cooling in Lead Halide Perovskites by Point Defects. J. Am. Chem. Soc. 2022, 144, 18126–18134.
- (86) Englman, R.; Jortner, J. The Energy Gap Law for Radiationless Transitions in Large Molecules. *Mol. Phys.* **1970**, *18*, 145–164.
- (87) Fu, J.; Xu, Q.; Han, G.; Wu, B.; Huan, C. H. A.; Leek, M. L.; Sum, T. C. Hot Carrier Cooling Mechanisms in Halide Perovskites. *Nat. Commun.* **2017**, *8*, 1300.
- (88) Richter, J. M.; Branchi, F.; Valduga de Almeida Camargo, F.; Zhao, B.; Friend, R. H.; Cerullo, G.; Deschler, F. Ultrafast Carrier Thermalization in Lead Iodide Perovskite Probed with Two-Dimensional Electronic Spectroscopy. *Nat. Commun.* **2017**, *8*, 376.
- (89) Yang, Y.; Ostrowski, D. P.; France, R. M.; Zhu, K.; van de Lagemaat, J.; Luther, J. M.; Beard, M. C. Observation of a Hot-Phonon Bottleneck in Lead-Iodide Perovskites. *Nat. Photonics* **2016**, 10, 53–59.
- (90) Li, M.; Fu, J.; Xu, Q.; Sum, T. C. Slow Hot-Carrier Cooling in Halide Perovskites: Prospects for Hot-Carrier Solar Cells. *Adv. Mater.* **2019**, *31*, No. 1802486.
- (91) Vogel, D. J.; Kryjevski, A.; Inerbaev, T.; Kilin, D. S. Photoinduced Single- and Multiple-Electron Dynamics Processes Enhanced by Quantum Confinement in Lead Halide Perovskite Quantum Dots. J. Phys. Chem. Lett. 2017, 8, 3032–3039.
- (92) Forde, R.; Inerbaev, T.; Hobbie, E. K.; Kilin, D. S. Excited-State Dynamics of a CsPbBr₃ Nanocrystal Terminated with Binary Ligands: Sparse Density of States with Giant Spin-Orbit Coupling Suppresses Carrier Cooling. *J. Am. Chem. Soc.* **2019**, *141*, 4388–4397.